Article:
Sun, Q, Magee, C, Jackson, CA-L et al. (2020) How do deep-water volcanoes grow? Earth and Planetary Science Letters, 542. 116320. ISSN: 0012-821X

https://doi.org/10.1016/j.epsl.2020.116320

How do deep-water volcanoes grow?

Qiliang Sun[1,2,3], Craig Magee[4], Christopher A-L. Jackson[5], Samuel J. Mitchell[6], Xinong Xie[1,3]

[1]Key Laboratory of Tectonics and Petroleum Resources, China University of Geosciences (Wuhan), Ministry of Education, Wuhan 430074, China;

[2]Laboratory for Marine Mineral Resources, Qingdao National Laboratory for Marine Science and Technology, Qingdao 266061, China;

[3]College of Marine Science and Technology, China University of Geosciences (Wuhan), Wuhan, Hubei 430074, PR China;

[4]Institute of Geophysics and Tectonics, School of Earth and Environment, University of Leeds, Leeds, LS2 9JT, UK;

[5]Basins Research Group (BRG), Department of Earth Science & Engineering, Imperial College, London, SW7 2BP, UK;

[6]Department of Earth Sciences, University of Bristol, Bristol, BS8 1RJ, UK

Abstract

Deep-water volcanoes are emplaced in water depths >1.0 km and are widespread along continental margins and in ocean basins. Whilst the external morphology of deep-water volcanoes can be mapped using bathymetric surveys, their internal structure and true volume remain enigmatic. It is thus difficult to determine how deep-water volcanoes grow. We investigate 13 Late Miocene-to-Quaternary, deep-water volcanoes that are imaged in 3D by seismic reflection data from the northern South China Sea, which allow us to quantify their external morphology and examine their internal structure. These deep-water volcanoes were emplaced in water depths >1.5 km, are relatively small (<3.0 km diameter, <0.56 km tall, and <0.92 km^3 in volume), and have steep slopes (up to 42°). Most of the volcanoes have erosional, 'crater-like' bases, infilled with sub-horizontal seismic reflections. These crater-like bases are overlain by downward-converging, conical seismic reflections delineating the classical volcano morphology. We suggest the crater-like bases formed by excavation of cold, wet, and poorly consolidated near-seabed

sediment during expulsion of hydrothermal fluid, and not by explosive magmatic eruptions or gravitational subsidence. Erupted igneous material infilled the precursor craters with the observed sub-horizontal layers, likely comprising hyaloclastites. After this initial phase of volcanism, the buildup of volcanic material produced layers that are now represented by the flank-parallel or downward-converging, conical seismic reflections. We suggest high hydrostatic pressures of >15 MPa, which are typical of water depths >1.5 km, inhibited degassing and fragmentation of ascending magma and thus erupted lava. This lack of degassing and fragmentation permitted effusive eruptions during the latter stages of volcanism. Our models for volcano growth in the deep submarine realm demonstrate the power of using 3D seismic data when investigating the internal structure and total volume of deep-water volcanoes.

Keywords: deep-water volcanoes, volcanism, extrusion dynamics, growth mechanism, erosion, South China Sea

1. Introduction

Volcanoes occur in a variety of plate boundary and intra-plate settings across Earth's surface. Determining how volcanoes grow is not only critical to predicting and mitigating volcanic hazards, but this understanding can also provide information on the underlying plumbing system structure (e.g., feeder and reservoir locations) and magma dynamics (e.g., composition and supply rate) (e.g., Moore and Clague, 1992; Arnulf et al., 2014; Clague et al., 2018). Volcanoes emplaced on land are typically well-studied and, by comparing their external morphology to similar neighboring edifices, we can infer they are broadly built through fluctuations between so-called summit- and diameter-prone growth (e.g., Moore and Clague, 1992; Rossi, 1996; Grosse et al., 2009; Karlstrom et al., 2018). Yet without direct access to volcano interiors, it is difficult to test growth models predicted from their external morphology alone. Examining ancient, (partially) eroded volcanoes provides some insight into how volcanoes are constructed, but modification of their original shape means we cannot assess relationship between internal structure and external morphology (e.g., Goto and Tomiya, 2019). By using traditional remote-sensing and/or field-based techniques, we can therefore either quantify the external morphology of uneroded

60 volcanoes, but not know their internal structure, or study the interiors of eroded volcanoes where
61 information on their original edifice shape has been lost. Our ability to only constrain either the
62 external morphology *or* internal structure of onshore volcanoes, but not both, limits our
63 understanding of how volcanoes grow.

64 Remote sensing data and lithostratigraphic analysis of well cores allow us to constrain the
65 external geometry and internal structure of the evolution of shallow- and deep-water volcanoes
66 (e.g., Smith, 1988; Magee et al., 2013; Cocchi et al., 2016; Buchs et al. 2018). In particular,
67 seismic reflection imaging of volcanoes provides a unique opportunity to resolve uncertainties
68 regarding volcano growth, given these data can image both the external morphology *and* internal
69 structure of volcanoes (e.g., Gatliff et al., 1984; Calves et al., 2011; Magee et al., 2013; Reynolds
70 et al., 2018; Sun et al., 2019). For example, by using 2D seismic reflection data offshore southern
71 Australia, Magee et al. (2013) showed trends in the external morphology of buried, shallow-water
72 shield volcanoes were consistent with growth via summit eruptions and a proportionate increase
73 in summit height and volcano diameters. Interpretation of reflections within the volcanoes reveal
74 the majority of volcanoes did indeed grow by a proportionate increase in summit height and basal
75 diameter (i.e. the layers were parallel to the volcano flanks) (Magee et al., 2013; see also Reynolds
76 et al., 2018). A similar seismic-based study of shallow-water volcanoes (water depth <200 m),
77 emplaced along the western Indian rifted margin, reveal they preferentially grew via increases in
78 diameter without a commensurate increase in summit height (Calves et al., 2011). Whilst seismic
79 reflection data have been used to unravel the growth of shallow-water volcanoes, few studies
80 have utilized these data to study the internal structure of deep-water (>1 km) volcanoes (e.g.,
81 Gatliff et al., 1984; Sun et al., 2019).

82 Discerning how deep-water volcanoes erupt and grow is critical for: (1) accurate assessment
83 of deep-water volcanic hazards (e.g. submarine landslides and associated tsunami; e.g. Staudigel
84 and Clague, 2010); (2) calculation of accurate eruptive and total volume estimates, which
85 contribute to understanding melting conditions in the underlying crust and/or mantle (e.g. Buchs
86 et al., 2018; Sun et al. 2019); and (3) determining the role of volcanoes in gas venting and
87 hydrothermal circulation (e.g. Planke et al., 2005). Importantly, high hydrostatic pressures in
88 deep-water settings, which can inhibit degassing, ascent rate, and fragmentation of magma, mean

89 the extrusion dynamics of deep-water volcanoes may fundamentally differ from their onshore and
90 shallow-water counterparts (e.g. Gregg and Fornari, 1998; Cas and Simmons, 2018; Carey et al.,
91 2018; Manga et al., 2018; Sun et al., 2019). These differences in eruption style and underlying
92 controls suggest we may not be able to simply apply our knowledge of volcanism in other,
93 subaerial or shallow water settings, to understand how deep-water volcanoes grow (e.g. Gregg
94 and Fornari, 1998; Manga et al., 2018). It is therefore necessary to image the internal structure of
95 deep-water volcanoes to reveal their growth history.
96 Here, we use 3D seismic reflection data to investigate 13 deep-water volcanoes located along
97 the continental margin of the northern South China Sea. These Late Miocene-Present volcanoes
98 were emplaced close to the Continent-Ocean Boundary (COB) in water depths >1.5 km. Our 3D
99 seismic reflection data allow us to map the external morphologies and internal structures of these
100 volcanoes in unprecedented detail. From our seismic reflection imaging, we propose the majority
101 of studied deep-water volcanoes grew through an initial phase of crater formation driven by
102 escape of hydrothermal fluids, which became infilled. Volcanic cones developed on top of these
103 infilled craters, or in two cases directly on undisturbed seabed sediment, primarily grew by
104 proportionate increases in summit height and basal diameter, thereby maintaining their slope
105 angle; some volcanoes appear to have grown by preferential addition of material to summit
106 regions. Although similar growth models have been proposed for volcanic cones in subaerial and
107 shallow marine settings, we demonstrate the deep-water volcanoes we study are relatively smaller
108 and have steeper slopes. We attribute the initial phase of crater formation and morphological
109 differences between deep-water volcanoes and those in other settings, to the unique physical
110 conditions under which deep-water volcanoes evolve. Our work shows seismic reflection data is
111 a powerful tool for unravelling volcano growth.
112
113 ## 2. Geological setting
114 The South China Sea is located in a complex tectonic region between the Eurasian, Pacific and
115 India-Australia plates (e.g. Briais et al., 1993; Franke et al., 2014; Li et al., 2014) (Fig. 1a). The
116 South China Sea evolved as a magma-poor rift, culminating in seafloor spreading, the onset of
117 which varied across the region (e.g. Clift et al., 2001; Cullen et al., 2010; Larsen et al., 2018).

Seafloor spreading began in the East Sub-basin in the early Oligocene (~33 Ma; Briais et al., 1993; Li et al., 2014), before the spreading center jumped to the Southwest Sub-basin in the late Oligocene (~25 Ma) (e.g. Franke et al., 2014). Spreading ceased sometime in the middle Miocene (~15.0-15.5 Ma; Briais et al., 1993; Li et al., 2014). Since the late Miocene (~10.5 Ma), tectonic activity in the northeastern part of South China Sea has been mainly driven by its collision with the Philippine Sea Plate (i.e. the Dongsha Event; e.g. Lüdmann and Wong, 1999).

The study area is located to the south of the Dongsha Islands in the northern South China Sea (Fig. 1a). Geological and geophysical studies (e.g. borehole, gravity, magnetic, and 2D and 3D seismic reflection data) indicate widespread Cenozoic volcanism across the northern South China Sea (e.g. Li and Liang, 1994; Yan et al., 2006; Zhao et al., 2016). From the early Paleocene to earliest Oligocene, before the onset of seafloor spreading, intermediate-acidic volcanoes were emplaced in a subaerial setting (Yan et al., 2006). From the Oligocene to middle Miocene, there was a compositional and environmental transition to the emplacement of mafic-to-intermediate volcanoes in shallow-water (<200 m) and subaerial settings (e.g. Yan et al., 2006; Lester et al., 2014) (Fig. 1a). Rapid post-emplacement subsidence led to these volcanoes being deeply buried (up to depths of 1.5 km) beneath the current seafloor (e.g. Zhao et al., 2016). Late Miocene and younger, intra-plate volcanoes (Figs. 1b-c) were emplaced close to the continent-ocean boundary (Clift et al., 2001; Sun et al., 2019). Recent IODP Expeditions 349/367/368 drilled several of these deep-water volcanoes in the South China Sea, revealing they are primarily basaltic (e.g. Li et al., 2014; Larsen et al., 2018), and that some were emplaced during continental breakup and directly covered by deep-water (>1.3 km) nanofossil-bearing clay sediments (Larsen et al., 2018). Many of the deep-water volcanoes, emplaced since the Late Miocene, feed long run-out lava flows that have irregular basal morphologies (Sun et al., 2019) (Figs. 1b-c). The volumes of these long run-out lavas appear equivalent to, or substantially greater than, that of the erupted material contained in the volcanoes themselves (Sun et al., 2019).

3. Datasets and methods

We use a time-migrated 3D seismic reflection dataset covering ~1150 km^2 to study the external morphology and internal structure of deep-water volcanoes in the South China Sea (Fig. 1a). The

147 data were acquired in 2012 using eight tuned air source guns, each with a volume of 8 × 20 in^3,
148 to produce a total shot volume of 8 × 160 in^3. Six 3000 m-long, 240-channel streamers with a
149 spacing of 12.5 m were used to tow the hydrophones. The data are zero-phase processed with
150 ordinary processing procedures (e.g. digital filtering, deconvolution, dynamic/static correction,
151 offset stack, etc.), and displayed with Society of Exploration Geophysicists (SEG) normal polarity.
152 A downward increase in acoustic impedance therefore corresponds to a positive reflection event
153 (red on displayed seismic profiles) and a downward decrease in acoustic impedance corresponds
154 to a negative reflection (black on displayed seismic profiles) (e.g. Brown, 2004).

155 The dominant frequency in the interval of interest (i.e. 0–400 m below the seabed) is ~40 Hz.
156 The estimated limit of separability within the deep-water strata (i.e. nanofossil-bearing clay)
157 encasing the volcanoes is ~14 m, based on a seismic velocity of 2.2 km/s for the sedimentary
158 rocks; this velocity is derived from nearby seismic refraction profiles (Yan et al., 2001; Wei et al.,
159 2011) (Fig. 1a). There are no seismic velocity data available for the studied deep-water volcanoes,
160 but we assume they have an interval velocity of the 4.0±1.0 km/s based on: (i) measured seismic
161 velocities of ~3.0-5.0 km/s for basaltic rocks (lava flows, volcaniclastic breccias and pyroclastics)
162 intersected by nearby boreholes (e.g. BY7-1 and IODP 1431) (Li et al., 2014; Zhao et al., 2016);
163 (ii) velocities of ~3.0-5.5 km/s obtained from seismic refraction profiles that cover other deep-
164 water volcanoes within the basin (Yan et al., 2001; Wei et al., 2011); (iii) typical seismic velocities
165 calculated from boreholes penetrating basaltic submarine volcanoes (~3.3-5.5 km/s) elsewhere
166 (Calvès et al., 2011); and (iv) the size of observed seismic velocity anomaly-induced 'pull-ups'
167 beneath the studied volcanoes (V7, V11, and V13, Fig. S1), caused by acoustic waves travelling
168 faster through hard, crystalline igneous rocks than the surrounding sedimentary strata (Jackson,
169 2012; Magee et al., 2013; Reynolds et al., 2018). With regard to the latter point, we calculate
170 interval velocities of 3.2-4.1 km/s for the three volcanoes (V7, V11, and V13), derived from the
171 magnitude of velocity pull-up artifacts (~82.7 ms - 161.3 ms TWT high) present in underlying
172 seismic reflections (Fig. S1):

173 $$\text{Vpi} = \frac{Ts \times Vps}{Ti}$$

174 where Vps (Vps = 2.2 km/s) and Vpi are the seismic velocities of encasing rocks/sediments and
175 igneous rocks; Ts and Ti are the seismic wave travel time in the encasing rocks/sediments and

igneous rocks, respectively (Fig. 2a).

Given a dominant frequency of ~40 Hz and an interval velocity of the 4.0±1.0 km/s, the estimated limits of separability and visibility of layers within the volcanoes is 25±6 m (λ/4) and 3.5±0.5 m (λ/30), respectively (Sun et al., 2019). When the volcanic structures are thicker than the estimated limit of separability, their top and base reflections can be distinguished. However, if their thickness lies between the limits of separability and visibility, they will appear as tuned reflection packages; i.e. reflections from their top and base interfere on their return to the surface and cannot be distinguished (e.g. Brown, 2004). Volcanic structures thinner than the limit of visibility will likely not be distinguishable from noise within the seismic data (Eide et al., 2017).

The volcanoes we study comprise two distinct components, involving a volcanic edifice and an underlying infilled crater-like base (Fig. 2b). We mapped three key seismic horizons: TV (top of volcano), BV (base of volcano), and the seabed (Figs. 3a-c). From these mapped horizons, we measured key geomorphologic parameters of the volcanoes, including diameter and height/depth of the edifices and crater-like bases (Fig. 2b). We define volcano thickness, which we also use to calculate volume, as the difference in height between TV and BV (Fig. 2b); volume estimates also take into account the irregular morphologies of TV and BV. Because the observed volcano flanks are rugged, we calculated average flank dips as height/(diameter/2) (Fig. 2b). In places, where volcanoes appear to merge, we constrain the plan-view extent of each edifice by distinguishing the location of minimum thickness between them (Fig. 3d). Errors in height, depth, volume, and flank dip measurements largely arise from uncertainties in the seismic velocities (4.0±1.0 km/s) used to undertake the depth conversion rather than measurement errors. The collected edifice and crater dimensions data allow us to better understand how much volcanic material may be underestimated by surficial remote-sensing techniques, and thus unaccounted for when calculating volumes of magma production. We also compare the geomorphologic characteristics of the volcanic edifices to volcanoes emplaced in different environments with varying composition, such as ocean basins (Basalt; Smith, 1988), subaerial volcanic arcs (Basalt - andesite; Grosse et al., 2009), submarine volcanic arcs (dacite, basalt-andesite; Wright et al., 2006) and shallow water (Basalt; Magee et al., 2013).

205 ## 4. Characteristics of the deep-water volcanoes

206 ### 4.1. Seismic expression

207 We mapped the top and bases, and thus constrained the thickness and volume of 13 volcanoes
208 (Figs. 3b-c; Table 1). In our seismic data, several volcanoes appear to have merged to form a
209 single, large edifice defined by multiple distinct summits (i.e. V4-V6 and V11-V12; Figs. 3b-c).
210 All the volcanoes are at least partly buried by a thin layer (<300 m) of Late Miocene- Quaternary
211 strata (Figs. 4-5; Table 1), with the tips of edifices (i.e. V6, V7, V9, V11, V12 and V13) breaching
212 the seabed (Figs. 3a, 4a-b, 4d, 4f). Except for V1, all volcanoes are encircled by moats that are
213 up to 75 m deep, and which, depending on their stratigraphic occurrence, are unfilled (i.e. moats
214 expressed at seabed), partly infilled, or fully filled (i.e. buried moats) (e.g. V6-V9; Figs. 3a, 4a-b,
215 4d-f, 5). The volcanoes are typically characterized by continuous-to-moderately continuous, high-
216 amplitude top reflections (i.e. TV), and discontinuous, primarily low-amplitude base reflections
217 (i.e. BV) (Figs. 4-5; Fig. S1). Occasionally BV is continuous and high-amplitude (e.g. V6; Fig.
218 4f). Projected boundaries dividing the crater-like bases and edifices of individual volcanoes occur
219 at different stratigraphic levels (Fig. 4). For example, the edifice-crater boundary for V12 is
220 coincident with the modern seabed, whilst for V9 the edifice-crater boundary is located ~50–100
221 ms TWT (~40-80 m) beneath the current seafloor (Figs 4a-b).

222 We identify two types of volcano bases: (i) crater-like bases that truncate underlying seismic
223 reflections (Figs. 4a-d); and (ii) relatively flat bases that are conformable with underlying strata
224 (e.g. V6 and V8; Figs. 4e-f). Based on these differences in basal geometry, we sub-divide the
225 volcanoes into two groups: (i) GP1 (11 volcanoes), which have crater-like bases (Figs. 4a-d); and
226 (ii) GP2 (2 volcanoes), which have strata-concordant bases (Figs. 4e-f). The bases of both groups
227 of volcanoes are located at various stratigraphic horizons, up to ~264 m beneath the seabed.
228 Seismic reflections directly beneath the volcanoes, as well as those below lavas emanating from
229 the volcanic edifices, have very low-amplitude compared to their typical seismic character away
230 from the overlying volcanoes (Fig. 5). These reflections beneath the volcanoes are also typically
231 disturbed and occasionally appear to be deflected upward relative to their regional dip (e.g. those
232 beneath V9 in Fig. 5).

233

234 **4.2. External volcano morphology and dimensions**

235 4.2.1. Volcano edifices

236 The volcanic edifices have circular to elliptical basal sections, with diameters of ~0.6–3.0 km
237 (average of ~1.3 km), covering areas of ~0.25-7.15 km^2 (Table 1). Edifice height ranges from
238 ~79±20 to 560±140 m (Figs. 3b, 6a; Table 1). There is a very weak (i.e. R^2 = ~0.21), positive
239 correlation between edifice diameter and height, with an average height:diameter ratio of 0.25
240 (Fig. 6a). Flanks are linear, convex-upward, or convex-downward, and are moderate-to-steep,
241 with dips of up to 42° (average dip of ~26°) (Figs. 4-5; Figs. S1-S2); most (nine) of the volcanoes
242 have slopes >20° (Table 1). Flank dip is weakly, negatively correlated with edifice diameter (R^2
243 = ~0.12; Fig. 6b) and weakly, positively correlated with height (R^2 = ~0.39; Fig. 6c). Overall,
244 edifice volumes range from ~0.0160±0.0040 to 0.9213±0.2303 km^3 and show a strong, positive
245 correlation to diameter (R^2 = ~0.94; Fig. 6d), but a weak correlation to height (R^2 = ~0.25; Fig.
246 6e) and no correlation with flank dip and volume (R^2 = ~0.06) (Fig. 6f).

247

248 4.2.2. Crater-like bases

249 The depth and diameter ranges of the crater-like bases are ~87±22 to 517±129 m and ~0.8 to
250 4.6 km, respectively, and only weakly, positively correlated (R^2 = ~0.20) (Fig. 7a; Table 1); their
251 volumes range from 0.0082±0.0021 to 0.8144±0.2036 km^3 (Table 1). The dips (5°-32°) of the
252 basal crater flanks are only weakly, negatively correlated to crater diameter (R^2 = ~0.29; Fig. 7b)
253 and very weakly, negatively correlated with depth (R^2 = ~0.17; Fig. 7c). Crater volume is
254 moderately-to-strongly, positively correlated (R^2 = ~0.65) with crater diameter but only weakly
255 correlated to crater depth (R^2 = ~0.22) and very weakly, negatively correlated with crater flank
256 dip (R^2 = ~0.16) (Figs. 7d-f).

257

258 4.2.3. Total volcano morphometrics

259 The heights of volcano edifices and depths of crater-like bases are weakly, positively correlated
260 (R^2 = ~0.36; Fig. 7g), whilst their diameters are moderately-to-strongly, positively correlated (R^2
261 = ~0.65; Fig. 7h). We note the diameters of the crater-like bases are typically greater than (e.g.
262 V5 and V11) or equal to (e.g. V10 and V13) those of their overlying edifices (Fig. 7h). These

differences in diameter mean that the *volumes* of crater-like bases are typically larger than those of the overlying edifices (Fig. 7i), e.g. by more than five times (e.g. V5; Table 1); the volumes of the crater-like bases and edifices are weakly, positively correlated (R^2 = ~0.23; Fig. 7i).

The average diameters, combining that of the edifices and crater-like bases, of individual volcanoes show a weak (R^2 = ~0.22), positive correlation to volcano thickness (Fig. 7j). The total volumes of volcanoes range from 0.0277±0.0070 to 1.2669±0.3167 km^3. Volcano thickness is only weakly (R^2 = ~0.28) positively correlated with total volcano volume (Fig. 7k). However, there is a strong (R^2 = ~0.88), positive correlation between total volcano volume and average diameter (Fig. 7j).

4.3. Internal architecture and seismic facies

We define two principal intra-volcano seismic facies (Fig. 4). Seismic facies 1 (SF1) is bound at its base by BV and predominantly comprises discontinuous, short, parallel to sub-parallel, moderate- to high-amplitude seismic reflections within the crater-like bases of GP1 (Figs. 4a-d). Reflections within SF1 appear broadly parallel with those of the surrounding sedimentary layers. Some outwardly dipping seismic reflections, which define broadly conical structures, are locally observed within the cores of SF1 (Figs. 4a-d). Overlying SF1, seismic facies 2 (SF2) constitutes the upper parts of all GP1 and GP2 volcanoes, broadly comprising stacked, continuous-to-moderately continuous, moderate-amplitude reflections that downlap onto SF1 or BV (Fig. 4). In most instances the internal SF2 reflections, where clearly observed, broadly parallel the outer margins of the volcanic edifices (e.g. Figs 4a, e-f); in some edifices the SF2 reflections converge down-dip (e.g. Fig. 4b).

5. Discussion

5.1 Age and environment of volcanism

Biostratigraphic data from nearby boreholes constrain the age of the nanofossil-bearing sedimentary sequences encasing the 13 mapped volcanoes, which have edifice bases that mark

291 the syn-eruptive seabed located at different stratigraphic levels (Figs. 4-5), and indicate volcanism
292 occurred periodically between the Late Miocene (e.g. ~6.3 Ma of V1; Sun et al., 2019) and
293 Quaternary. Analysis of ODP (Site 1146) and IODP (Site U1501) data reveal that, at least since
294 the Early Miocene (~23 Ma) and throughout this prolonged period of intermittent volcanism, the
295 study area was a deep-water (>1.0 km) environment (e.g. Clift et al., 2001; Li et al., 2014; Larsen
296 et al., 2018). Because the mapped volcanoes are within an area characterized by a present water
297 depth of >1.3 km, and the subsidence-corrected, syn-emplacement Miocene-Quaternary sea level
298 was ~200 m higher than it is today (Xu et al., 1995), we consider it likely that eruptions occurred
299 in water depths >1.5 km; these water depths correspond to overlying hydrostatic pressures of >15
300 MPa.
301
302 **5.2. Volcano formation and growth**
303 Most of the thirteen mapped volcanoes (11 of 13) can be sub-divided into an edifice and a
304 crater-like base (Figs. 4a-d, 5). These crater-like bases truncate the underlying stratigraphic
305 reflections and are infilled by sub-horizontal reflections, onto which a conical edifice is developed
306 (Figs. 4a-d, 5). Here we discuss how each of these features relates to the initiation and growth of
307 these deep-water volcanoes.
308
309 5.2.1. Formation of crater-like bases
310 Crater-like bases have been observed beneath volcanoes and hydrothermal vents in subaerial
311 and shallow-water settings, and their formation has primarily been attributed to disaggregation
312 and material removal during explosive eruptions (e.g. Planke et al., 2005; Wright et al., 2006;
313 Geyer and Martí, 2008). Alternatively, crater-like bases could form by the collapse of subsurface
314 conduits following magma extraction and subsidence of overlying material (e.g. Walker, 1993;
315 Geyer and Martí, 2008) and/or post-emplacement gravitational subsidence in response to volcano
316 loading (e.g. Moore and Clague, 1992; de Silva and Lindsay, 2015); depressions generated by
317 these subsidence processes are expected to host inward-dipping layers (e.g. de Silva and Lindsay,
318 2015). We consider it unlikely that the crater-like bases documented here (e.g., Figs 4a-d) formed
319 by subsidence because: (i) gravitational subsidence driven by volcano loading could not produce

craters volumetrically larger than, and which occasionally extend beyond the footprint of, the overlying edifices (Moore and Clague, 1992; de Silva and Lindsay, 2015) (Fig. 7i; Table 1); (ii) volcano loading will cause underlying reflections to sag and will *not* produce craters that truncate and erode underlying strata (Figs. 4a-d); and (iii) the sub-horizontal reflections observed within the crater-like bases are inconsistent with collapse of pre-existing strata into evacuated magma conduits or deformation imposed by the volcano load (Figs. 4a-d).

By ruling out subsidence as a mechanism for driving crater formation, our observed truncation and erosion of underlying strata by the craters may suggest they formed via an initial phase of explosive activity (e.g. Planke et al., 2005; Wright et al., 2006; Geyer and Martí, 2008). However, whilst evidence for explosive volcanism (e.g. pyroclast occurrence) has been documented in silicic, volatile-rich deep-water settings, high hydrostatic pressures caused by large water columns (e.g. >1.0 km) are expected to prevent substantial exsolution of volatiles from magma and thereby inhibit explosive eruptions (e.g. Walker, 1993; de Silva and Lindsay, 2015; Carey et al., 2018; Cas and Simmons, 2018). Although we lack the well data required to test whether the crater-infilling-material was generated by explosive volcanic activity, we consider it plausible that the deep-water emplacement (>1.5 km) and the basaltic, inferred volatile-poor nature of magma extruded from these volcanoes may have restricted a namely "explosive" eruption style. In particular, the interplay of the deep-water setting and magma composition may have led to primarily effusive eruptions or rapid magma extrusion into the water column in a "non-explosive" manner, e.g. such as suggested for high mass eruption rates by Manga et al. (2018). If explosive activity was inhibited, a different mechanism for producing the observed erosive craters is required.

Given the sub-horizontal seismic reflections (i.e. SF1) infilling the craters and truncation of underlying strata by the basal surface, we suggest the crater-like bases could have formed in response to the escape of magma-related hydrothermal fluids (e.g. fluids from magma and/or heated pore fluids from the surrounding sediments). We propose that fluid escape disaggregated and excavated the weak, near-seabed sediments via a similar process to that inferred for ancient, seismically-imaged hydrothermal vents (e.g. Planke et al., 2005; Buarque et al., 2016). Considering expelled, fine-grained sediments are likely to be removed by bottom currents (e.g.

Judd and Hovland, 2007), we suggest the crater may have been infilled by sub-horizontal packages composed of either: (i) erupted dense material that settles out of the water column (i.e. it is not affected by bottom currents), perhaps forming layers of hyaloclastites; and/or (ii) material eroded from the depression flanks and deposited within the crater. The process we infer for the formation of the crater-like bases is similar to the generation of deep-water pockmarks, which are usually of kilometer-scale and infilled by sub-horizontal sedimentary strata (e.g. Judd and Hovland, 2007). Further exploration of the material filling these basin-like structures by drilling and coring would help clarify the style and nature of the eruptive activity and crater formation.

Regardless of the process(es) driving crater formation, the absence of crater-like bases beneath GP2 edifices indicates volcanism did not always involve near-seabed excavation and was site specific (Figs. 4e-f). It is difficult to determine exactly what factors (e.g. seabed cohesivity and porosity, water depth, mass eruption rate, magma composition and volatile content) controlled the initial emplacement styles of the GP1 and GP2 volcanoes solely from the geophysical data we use here.

5.2.2. Model of volcano growth

Volcano geometry is influenced by the interplay of constructive (e.g. dyke intrusion and stacking of lava flows) and destructive processes (e.g. flank collapse and erosion) (e.g. Annen et al., 2001; Kervyn et al., 2009; Magee et al., 2013). To evaluate edifice growth, field- and remote sensing-based studies broadly rely on the assumption that, in any given volcanic field or setting, small volcanoes develop into large volcanoes (e.g. Walker, 1993; de Silva and Lindsay, 2015). Patterns in volcano morphometry have therefore been used to infer growth models (e.g. Rossi, 1996; Calvès et al., 2011; Magee et al., 2013; Karlstrom et al., 2018). From these morphometric data, the following growth models for various volcanoes from subaerial and shallow marine settings have been proposed (Fig. 8): (i) proportional increase in summit height and basal diameter, maintaining flank dip (Magee et al., 2013; Figs 8b, f); (ii) preferential addition of material to the summit area and upper volcano flanks, whilst the diameter remains consistent and flank dip increases with time (Magee et al., 2013; Figs 8c, f); (iii) lateral progradation of the edifice flanks while summit height is fixed, such that flank dip decreases with time (Calvès et al., 2011; Figs

8d, f); and (iv) maintenance of a proportional increase in summit height and basal diameter with time, interrupted by a short-stage of lateral progradation of the edifice flanks (Rossi, 1996; Figs 8e, f). However, these growth models derived from volcano morphometry data are difficult to test because we cannot easily access and evaluate the internal 3D structure of volcanoes. Seismic reflection data uniquely allows us to image volcano interiors in 3D, meaning we can interrogate how edifices build up through time by mapping internal layers (Magee et al. 2013; Sun et al., 2019). Here, we compare the internal architecture of our deep-water volcanoes to growth models from those emplaced in subaerial and shallow marine conditions (Fig. 8), and discuss potential environmental controls on the differences we recognize in their geometry and evolution.

The internal seismic facies variations we recognize within our GP1 volcanoes differ from the seismic facies observed within monogenetic volcanoes that are mainly characterized by homogeneous seismic reflections (e.g. Reynolds et al., 2018). These facies differences suggest the GP1 volcanoes were instead formed through multiple eruptive events (i.e. they are polygenetic) and we propose they likely developed in three stages (Fig. 9): (Stage 1) during the first stage, crater-like bases formed through the explosive expulsion of hydrothermal fluids (see Section 5.2.1); (Stage 2) crater infilling through eruption of material and/or mass wasting of crater flanks, forming the aggradational SF1 facies; (Stage 3) construction of a broadly conical edifice on a relatively flat surface, following crater infilling, through summit eruptions that promoted vertical and lateral growth as evidenced by the positive correlation between volcano height and basal diameter, and the parallelism between their external morphology and internal SF2 reflections (cf. Figs. 4, 6a, 8a-b, f). Down-dip convergence of internal SF2 reflections in some volcanoes (e.g. V12; Fig. 4b) suggests that, for some edifices, vertical aggradation through accumulation of erupted material at the summit may have outpaced lateral expansion of the basal diameter (e.g. Figs. 8a, c, f) (Vail et al. 1977; Magee et al. 2013); i.e. in this scenario, little erupted material reached the base flanks of the volcano, perhaps because eruption rate was low and episodic. The growth of some volcanoes by vertical aggradation may explain why flank dips of the GP1 population correlate moderately positively with volcano height, but not basal diameter (Figs. 6b-c). During Stage 2 or Stage 3, after full or partial infilling of the crater-like base, intrusions feeding summit eruptions may have modified the core of SF1 to form the conical structures that are locally

407 observed (Figs. 4a-d, 9).

408 GP2 volcanoes lack crater-like bases but otherwise appear similar to GP1 (Figs 4 and 6); i.e.
409 the volcanic materials contained in the GP2 volcanoes were expelled directly onto the paleo-
410 seabed, feeding a volcano that grew both vertically and laterally (Stage 3; Fig. 9). The narrow,
411 low-amplitude zone directly beneath the volcanoes and associated deformations (e.g. deflected-
412 upward seismic reflections) suggest that dykes or faults may have served as magma ascent
413 pathways (MP) (Fig. 5). However, these upward-deflected seismic reflections may also be
414 possibly interpreted as seismic artefacts (i.e. velocity pull-ups) that are caused by the overlying
415 thick, high-density volcanic rocks.

416

417 ### 5.2.3 Controls on edifice morphology

418 Compared to subaerial and shallow-water basaltic volcanoes, as well as moderate- to deep-
419 water (0.9-3 km) andesitic-basaltic volcanoes, the deep-water basaltic volcanoes we study: (i) are
420 ~41–427 times (in volumes) smaller than basaltic and basaltic-andesitic volcanoes from
421 elsewhere (Fig. 6a, d-e; Table S1); (ii) display similar positive correlations between height,
422 diameter, and volume, implying volcano growth broadly involved a proportionate increase in
423 summit height and basal diameter (Fig. 8-9) (e.g., Magee et al., 2013); but (iii) have steeper flanks
424 (most of them >20°), with some volcanoes evidently growing via preferential vertical aggradation
425 (Fig. 6b-c). We tentatively suggest that the small size and steeper flanks we observe likely reflect
426 differences in the environment of emplacement (e.g., water depth) and seabed lithology. Below
427 we consider how mass eruption rate and magma volatile content may control the
428 geomorphological characteristics of volcanoes in this study.

429 The magnitude, duration, and steadiness of eruption rate influence the distribution of extruded
430 material (e.g. de Silva and Lindsay, 2015; White et al., 2015). For example, low eruption rates
431 drive lava to move slowly over short distances (e.g. Rossi, 1996) and, thus, erupted materials are
432 more likely to accumulate around the vents/upper flanks and form high-angle slopes; i.e. growth
433 is via preferential vertical aggradation. Low eruption rates could explain the steep slopes of the
434 volcanoes we study, and may relate to the limited magma supply during post-rift volcanism (e.g.
435 Yan et al., 2006; Li et al., 2014) and/or volatile undersaturation in the basaltic parental magma.

436 Episodic, shorter-duration emplacement of lava (as opposed to a single event) would also build
437 notably steeper flanked volcanoes, as demonstrated in experiments by Fink et al. (1993). However,
438 we note that the presence of long run-out lava flows flanking the volcano edifices (>9.0 km long)
439 likely indicates eruption rates varied significantly through time, with intermittent periods of short-
440 lived, high eruption rates of, possibly, volatile-enriched magma feeding the longest run-out flows
441 (Sun et al., 2019) (Fig. 5). In addition to the low mass eruption rates, volatile-undersaturated lavas
442 (as primarily inferred here) have higher cooling rates,higher glass transition temperatures and
443 higher viscosities, and thus, lava may quench and build-up more proximal to the eruptive source
444 (Del Gaudio et al., 2007).

445 Because of high hydrostatic pressure, wet, cold, and unconsolidated sediments, and the overall
446 magma-deficient (low eruption rate and magma supply), post-rift setting during the Late Miocene,
447 the deep-water volcanoes documented here geomorphologically and genetically differ to their
448 subaerial and shallow-water counterparts in other tectonic environments (Fig. 6). In future,
449 physical and geochemical studies of eruptive products, particularly within GP1 volcanoes, may
450 help resolve the unusual morphologies and eruptive mechanisms within this tectonic setting.

451

452 ## 6. Conclusion

453 We use 3D seismic reflection data to investigate the three-dimensional structure of thirteen
454 Late Miocene-to-Quaternary deep-water volcanoes. Two groups of volcanoes, one with (GP1)
455 and one without (GP2) crater-like bases, are identified. Internally, these volcanoes comprise two
456 dominant seismic facies types that document volcano growth processes. We are able to investigate
457 the relationship between the external morphology and internal structure of deep-water volcanoes,
458 and thereby build growth models for these hitherto poorly understood volcanic structures. The
459 growth of most of the volcanoes is defined by two main stages: crater formation and infilling,
460 likely initiated by the escape of hydrothermal fluids, and subsequent construction of an overlying
461 conical edifice. Importantly, recognition of crater-like bases beneath the volcanoes implies the
462 volume of modern deep-water volcanoes, which are typically quantified by bathymetric surveys,
463 may be grossly underestimated as the volcanoes may not have a flat, seabed-parallel base. In this
464 study, most of the deep-water volcanoes have edifice volumes less than the underlying craters.

Our growth models suggest the morphology of the studied deep-water volcanoes were primarily controlled by the high hydrostatic pressure occurring in the deep-water setting, the volatile-poor nature of the parent magma, and variable magma supply due to the post-rift tectonic setting. In particular, these factors led to erupted material primarily accumulating near the summit and on the upper flanks of the volcanoes, meaning they have relatively smaller sizes (basal diameters, heights and volumes) and are characterized by slopes steeper than that typically seen in their subaerial, shallow-water, and deep-water arc-related counterparts. This study adds a unique dataset to the global database of submarine volcano morphologies. Moreover, this study also highlights that 3D seismic surveys could help revise previous estimates of submarine volcano or seamount volumes and morphologies, and further our understanding of submarine volcanoes that are already relatively-well studied.

Acknowledgment

This work was supported by the National Scientific Foundation of China (Grant Nos. 41676051 and 41372112), the Programme of Introducing Talents of Discipline to Universities (No. B14031) and the China Scholarship Council (201906415013). We thank the China National Offshore Oil Company for permission to release the data. The reflection seismic data may be requested from this Company (https://www.cnoocltd.com/). Editor Jean-Philippe Avouac, and journal reviewers Deniz Cukur, Tim Henstock and an anonymous reviewer are thanked for their invaluable comments and suggestions.

References

Annen, C., Lénat, J.F., Provost, A., 2001. The long-term growth of volcanic edifices: numerical modelling of the role of dyke intrusion and lava flow emplacement. J. Volcanol. Geotherm. Res. 105, 263-289, https://doi.org/10.1016/S0377-0273(00)00257-2.

Arnulf, A.F., Harding, A.J., Kent, G.M., Carbotte, S.M., Canales, J.P., Nedimović, M.R., 2014. Anatomy of an active submarine volcano. Geology, 42, 655-658, https://doi.org/10.1016/10.1130/G35629.1.

Briais, A., Patriat, P., Tapponnier, P., 1993. Updated interpretation of magnetic anomalies and seafloor spreading stages in the South China Sea: Implications for the Tertiary tectonics of Southeast Asia. J. Geophys. Res. 98, 6299-6328, https://doi.org/10.1029/92JB02280.

Brown, A. R., 2004. Interpretation of three-dimensional seismic data: AAPG Memoir 42, 6thed. SEG Investigations in Geophysics.

Buarque, B.V., Barbosa, J.A., Magalhães, J.R.G., Oliveira, J.T.C., Filho, O.J.C., 2016. Post-rift volcanic structures of the Pernambuco Plateau, northeastern Brazil. J. S. Am. Earth, Sci. 70, 251-267, http://dx.doi.org/10.1016/j.jsames.2016.05.014.

Buchs, D.M., Williams, R., Sano, S., Wright, V.P., 2018. Non-Hawaiian lithostratigraphy of Louisville seamounts and the formation of high-latitude oceanic islands and guyots. J. Volcanol. Geotherm. Res. 356, 1-23, https://doi.org/10.1016/j.jvolgeores.2017.12.019.

Calvès, G., Schwab, A.M., Huuse, M., Clift, P.D., Gaina, C., Jolley, D., Tabrez, A.R., Inam, A., 2011. Seismic volcanostratigraphy of the western Indian rifted margin: The pre-Deccan igneous province. J. Geophys. Res. 116, B01101, https://doi.org/10.1029/2010JB000862.

Carey, R., Soule, S.A., Manga, M., White, J.D.L., McPhie, J., Wysoczanski, R., Jutzeler, M., Tani, K., Yoerger, D., Fornari, D., Caratori-Tontini, F., Houghton, B., Mitchell, S., Ikegami, F., Conway, C., Murch, A., Fauria, K., Jones, M., Cahalan, R., and McKenzie, W., 2018. The largest deep-ocean silicic volcanic eruption of the past century. Sci. Adv. 4, e1701121, https://doi.org/10.1126/sciadv.1701121.

Cas, R.A.F., Simmons, J., 2018. Why deep-water eruptions are so different from subaerial eruptions? Front. Earth Sci. 6, https://doi.org/10.3389/feart.2018.00198.

Clague, D.A., Paduan, J.B., Dreyer, M.B., Chadwick Jr, D.M., Rubin, K.R., Perfit, M.R., Fundis, A.T., 2018. Chemical Variations in the 1998, 2011, and 2015 Lava Flows From Axial Seamount, Juan de Fuca Ridge: Cooling During Ascent, Lateral Transport, and Flow. Geochem. Geophys. Geosyst. 19, 2915-2933, https://doi.org/10.1029/2018GC007708.

Clift, P.D., Lin, J., and ODP Leg 184 Scientific Party, 2001. Patterns of extension and magmatism along the continent-ocean boundary, South China margin. Geological Society, London, Special Publications, 187, 489-510, https://doi.org/10.1144/GSL.SP.2001.187.01.24.

Cullen, A., Reemst, P., Henstra, G., Gozzard, S., Ray, A., 2010. Rifting of the South China Sea: new perspectives. Petrol. Geosci. 16, 273-282, https://doi.org/10.1144/1354-079309-908.

Del Gaudio, P., Behrens, H., Deubener, J., 2007. Viscosity and glass transition temperature of hydrous float glass. J. Non-cryst. Solids. 353, 223-236, https://doi.org/10.1016/j.jnoncrysol.2006.11.009.

de Silva, S., Lindsay, J.M., 2015, Primary volcanic landforms. In: Sigurdsson, H., Houghton, B.F., McNutt, S.R., Rymer, H., Stix, J. (eds), Encyclopedia of volcanoes, 2nd ed. Academic, London, pp 273-297, http://dx.doi.org/10.1016/B978-0-12-385938-9.00015-8.

Eide, C.H., Schofield, N., Jerram, D.A., Howell, J., 2017. Basin-scale architecture of deeply emplaced sill complexes: Jameson Land, East Greenland. J. Geol. Soc. London. 174, 23-40, https://doi.org/10.1144/jgs2016-018.

Fink, J.H., Bridges, N.T., Grimm, R.E., 1993. Shapes of Venusian “pancake” domes imply episodic emplacement and silicic composition. Geophys. Res. Lett. 20,261-264, https://doi.org/10.1029/92GL03010.

Franke, D., Savva,D., Pubellier, M., Steuer, S., Mouly, B., Auxietre, J., Meresse, F., Chamot-Rooke, N., 2014. The final rifting evolution in the South China Sea. Mar. Petrol. Geol. 58, 704-720, https://doi.org/10.1016/j.marpetgeo.2013.11.020.

Geyer, A., Martí, J., 2008. The new worldwide collapse caldera database (CCDB): a tool for studying and understanding caldera processes. J. Volcanol. Geotherm. Res. 175, 334-354, http://dx.doi.org/10.1016/j.jvolgeores.2008.03.017.

Goto, Y., Tomiya, A., 2019. Internal Structures and Growth Style of a Quaternary Subaerial Rhyodacite Cryptodome at Ogariyama, Usu Volcano, Hokkaido, Japan. Front. Earth Sci. 7, 66, https://doi.org/10.3389/feart.2019.00066.

Gregg, T.K.P., Fornari, D.J., 1998. Long submraine lava flows: Observations and results from numerical modeling. J. Geophys. Res. 103, 27517-27531, https://doi.org/10.1029/98JB02465.

Grosse, P., van Wyk de Vries, B., Petrinovic, I.A., Euillades, P.A., Alvarado, G.E., 2009. Morphometry and evolution of arc volcanoes. Geol. Soc. Am. 37, 651-654, https://doi.org/10.1130/G25734A.1.

Jackson, C.A.-L., 2012. Seismic reflection imaging and controls on the preservation of ancient sill-fed magmatic vents. J. Geol. Soc. London 169, 503-506, https://doi.org/10.1144/0016-76492011-147.

Judd, A.G., and Hovland, M., 2007, Seabed Fluid Flow: The Impact on Geology, Biology and the Marine Environment. Cambridge University Press, Cambridge, pp. 163-178.

Karlstrom, L., Richardson, P.W., O'Hara, D., Ebmeier, S.K., 2018. Magmatic Landscape Construction. J. Geophys. Res.- EARTH, 123, 1710-1730, https://doi.org/10.1029/2017JF004369.

Kervyn, M., Ernst, G.G.J., van Wyk de Vries, B., Mathieu, L., Jacobs, P., 2009. Volcano load control on dyke propagation and vent distribution: Insights from analogue modelling. J. Geophys. Res. 114, B03401, https://doi.org/10.1029/2008JB005653.

Larsen, H.C., Mohn, G., Nirrengarten, M., Sun, Z., Stock, J., Jian, Z., Klaus, A., Alvarez-Zarikian, C.A., Boaga, J., Bowden, S.A., Briais, A., Chen, Y., Cukur, D., Dadd, K., Ding, W., Dorais, M., Ferré, E.C., Ferreira, F., Furusawa, A., Gewecke, A., Hinojosa, J., Höfig, T.W., Hsiung, K.H., Huang, B., Huang, E., Huang, X.L., Jiang, S., Jin, H., Johnson, B.G., Kurzawski, R.M., Lei, C., Li, B., Li, L., Li, Y., Lin, J., Liu, C., Liu, C., Liu, Z., Luna, A.J., Lupi, C., McCarthy, A., Ningthoujam, L., Osono, N., Peate, D.W., Persaud, P., Qiu, N., Robinson, C., Satolli, C., Sauermilch, I., Schindlbeck, J.C., Skinner, S., Straub, S., Su, X., Su, C., Tian, L., van der Zwan, F.M., Wan, S., Wu, H., Xiang, R., Yadav, R., Yi, L., Yu, P.S., Zhang, C., Zhang, J., Zhang, Y., Zhao, N., Zhong, G., Zhong, L., 2018. Rapid transition from continental breakup to igneous oceanic crust in the South China Sea. Nat. Geosci. 11, 782-789, https://doi.org/10.1038/s41561-018-0198-1.

Lester, R., Van Avendonk, H.J.A., McIntosh, K., Lavier, L., Liu, C.S., Wang, T.K., Wu, F., 2014. Rifting and

563 magmatism in the northeastern South China Sea from wide-angle tomography and seismic reflection imaging.
564 J Geophys. Res. 119, 2305-2323, https://doi.org/10.1002/2013JB010639.
565 Li, P., and Liang, H., 1994. Cenozoic magmatism in the Pearl River Mouth Basin and its relationship to the basin
566 evolution and petroleum accumulation. Guangdong Geology, 9, 23-34.
567 Li, C.F., Xu, X., Lin, J., Sun, Z., et al., 2014. Ages and magnetic structures of the South China Sea constrained by
568 the deep tow magnetic surveys and IODP Expedition 349. Geochem. Geophys. Geosyst. 15, 4958-4983,
569 https://doi.org/10.1002/2014GC005567.
570 Lüdmann, T., Wong, H., 1999. Neotectonic regime on the passive continental margin of the northern South China
571 Sea. Tectonophysics 311, 113-138, https://doi.org/10.1016/S0040-1951(99)00155-9.
572 Magee, C., Hunt-Stewart, E., Jackson, C.A.-L., 2013. Volcano growth mechanisms and the role of sub-volcanic
573 intrusions: Insights from 2D seismic reflection data. Earth Planet. Sci. Lett. 373, 41-53,
574 https://doi.org/10.1016/j.epsl.2013.04.041.
575 Manga, M., Fauria, K.E., Lin, C., Mitchell, S.J., Jones, M., Conway, C.E., Degruyter, W., Hosseini, B., Carey, R.,
576 Cahalan, R., Houghton, B.F., White, J.D.L., Jutzeler, M., Soule, S.A., Tani, K., 2018. The pumice raft-forming
577 2012 Havre submarine eruption was effusive. Earth Planet. Sci. Lett. 489, 49-58,
578 https://doi.org/10.1016/j.epsl.2018.02.025.
579 Moore, J.G., Clague, D.A., 1992. Volcano growth and evolution of the island of Hawaii. Geol. Soc. Am. Bull.
580 104, 1471-1484, https://doi.org/10.1130/0016-7606(1992)104<1471:VGAEOT>2.3.CO;2.
581 Planke, S., Rasmussen, T., Rey, S.S., Myklebust, R., 2005. Seismic characteristics and distribution of volcanic
582 intrusions and hydrothermal vent complexes in the Vøring and Møre Basins. In: Dore, A.G., Vining, B. (Eds.),
583 Proceedings of the 6th Petroleum Geology Conference on Petroleum Geology: N.W. Europe and Global
584 Perspectives, pp. 833-844.
585 Reynolds, P., Schofield, N., Brown, R.J. Holford, S.P., 2018. The architecture of submarine monogenetic
586 volcanoes-insights from 3D seismic data. Bas. Res. 30, 437-451, https://doi.org/10.1111/bre.12230.
587 Rossi, M.J., 1996. Morphology and mechanism of eruption of post glacial shield volcanoes in Iceland. Bull.
588 Volcanol. 57, 530-540, https://doi.org/10.1007/BF00304437.
589 Smith, D.K., 1988. Shape analysis of Pacific seamounts. Earth Planet. Sci. Lett. 90, 457-466.
590 Staudigel, H., Clague, D.A., 2010. The geological history of deep-sea volcanoes: biosphere, hydrosphere, and
591 lithosphere interactions. Oceanography, 23, 58-71, https://doi.org/10.5670/oceanog.2010.62.
592 Sun, Q.L., Jackson, C.A-L., Magee, C., Mitchell, S.J., Xie, X.N., 2019. Extrusion dynamics of deep-water
593 volcanoes. Solid Earth Discuss., https://doi.org/10.5194/se-2019-87.
594 Vail, P.R., Todd, R.G., Sangree, J.B., 1977. Seismic stratigraphy and global changes in sea level, part 5. In: Payton,
595 C.E. (Ed.), Seismic Stratigraphy: Application to Hydrocarbon Exploration, 8th edition. American Association
596 of Petroleum Geologists, pp. 99-116.

Walker, G.P.L., 1993. Basaltic-volcano systems. In: Magmatic Processes and Plate Tectonics, edited by Pritchard, H.M., Alabaster, T., Harris, N.B.W., Neary, C.R., Geological Society Special Publication, 76: 3-38.

Wright, I.C., Worthington, T.J., Gamble, J.A., 2006. New multibeam mapping and geochemistry of the 30°–35° S sector, and overview, of southern Kermadec arc volcanism. J. Volcanol. Geotherm. Res., 149, 263-296, https://doi.org/10.1016/j.jvolgeores.2005.03.021.

Wei, X.D., Ruan, A.G., Zhao, M.H., Qiu, X.L., Li, J.B., Zhu, J.J., Wu, Z.L., and Ding, W.W., 2011. A wide-angle OBS profile across the Dongsha uplift and Chaoshan depression in the mid-northern South China Sea. Chinese Journal of Geophysics, 54, 3325-3335, https://doi.org/10.3969/j.issn.0001-5733.2011.12.030.

White, J.D.L., McPhie, J., Soule, S.A., 2015. Submarine lavas and hyaloclastite. In: Sigurdsson, H., Houghton, B.F., McNutt, S.R., Rymer, H., Stix, J. (eds), Encyclopedia of volcanoes, 2nd edn. Academic, London, pp 363–375, http://dx.doi.org/10.1016/B978-0-12-385938-9.00019-5.

Xu, S.C., Yang, S.K., Huang, L.F., 1995. The application of sequence stratigraphy to stratigraphic correlation. Earth Science Frontiers, 2, 115-123.

Yan, P., Deng, H., Liu, H.L., Zhang, Z., Jiang, Y., 2006. The temporal and spatial distribution of volcanism in the South China Sea region. J. Asian Earth Sci. 27, 647-659, https://doi.org/10.1016/j.jseaes.2005.06.005.

Yan, P., Zhou, D., and Liu, Z.S., 2001. A crustal structure profile across the northern continental margin of the South China Sea. Tectonophysics, 338, 1-21, https://doi.org/10.1016/S0040-1951(01)00062-2.

Yang, S., Qiu, Y., and Zhu, B., 2015, Atlas of Geology and Geophysics of the South China Sea: China Navigation Publications, Tianjin.

Zhao, F., Alves, T.M., Wu, S.G., Li, W., Huuse, M., Mi, L.J., Sun, Q.L., Ma, B.J., 2016. Prolonged post-rift magmatism on highly extended crust of divergent continental margins (Baiyun Sag, South China Sea). Earth Planet. Sci. Lett. 445, 79-91, https://doi.org/10.1016/j.epsl.2016.04.001.

Zou, H.P., Li, P.L., Rao, C.T., 1995. Geochemistry of Cenozoic volcanic rocks in Zhujiangkou basin and its geodynamic significance. Geochemica, 24, 33-45.

Figure Captions

Figure 1: (a) Geological setting of the study area. Red polygonal line located to the south of Dongsha Islands is the 3D seismic survey. Top left: regional setting of the South China Sea. It is bounded by the Red River Strike-slip faults (RRFs) to the west and by the subduction trench (Manila Trench) to the east. Northern South China Sea is marked with black square. Igneous rocks

629 with ages from exploration wells and seamount dredges are marked with blue circles/rings (Jin,
630 1989; Li and Liang, 1994; Zou et al., 1995). Crustal structure profiles (OBS1993 (Yan et al., 2001)
631 and OBS2006-3 (Wei et al., 2011)) are marked with pink solid lines. ODP sites 1145 and1146,
632 IODP site U1501 and location of Figure 3 are also labeled. The base map is modified from Yang
633 et al. (2015) and Sun et al. (2019); (b) and (c) Regional seismic strata of the study area. Volcanic
634 materials are mainly located in the shallow level (0-300 m) of post-rifting strata. See location in
635 (a).
636
637 Figure 2: (a) Schematic diagram of the calculation method for igneous velocity within the volcano
638 and surrounding sediments; (b) Schematic diagram of geomorphic parameters measured in this
639 study, using an example volcano with an identified crater-like base and overlying edifice. Note
640 that the travel-time distances between the volcano summit and its base (Ts), or the top of the
641 velocity pull-up (Ti), were measured *within* the volcano edifices.
642
643 Figure 3: (a) Present seabed morphologies of the study area, interpreted from the 3D seismic data.
644 The landmark areal projections of buried or partly buried volcanoes are marked; (b) Thickness
645 (and thus, height) of volcano edifices in the study area; (c) Thickness (and thus, depth) of volcano
646 craters in the study area; (d) Total thickness of the volcanoes, calculated from the vertical addition
647 of (b) and (c). The boundaries of merged volcanoes are marked. 100 ms (twt) = ~200 m.
648
649 Figure 4: (a) - (d): Seismic characteristics of volcanoes (GP1). (a) Volcano 9 (V9) and its line
650 drawing; (b) Volcano 12 (V12) and its line drawing; (c) Volcano 1 (V1) and its line drawing; (d)
651 Volcano 7 (V7) and its line drawing. (e) - (f): Seismic characteristics of volcanoes (GP2). (e)
652 Volcano 8 (V8) and its line drawing; (f) Volcano 6 (V6) and its line drawing. 150 ms (twt) for
653 volcano is equal to ~300 m. TV = top of volcano; PS = present seabed (solid pink line); PLS =
654 paleo-seabed (solid green line); IS = inferred present seabed (dashed pink line); SF1 = seismic
655 facies 1; SF2 = seismic facies 2; VE. = vertical exaggeration. See locations in Fig. 3a.
656
657 Figure 5: 3D seismic profile crosses through V8, V9 and V10. The igneous pathways underneath

658 the volcanoes are narrow, vertical structures (dashed arrows) and the surrounding strata are
659 slightly pushed upward, suggesting them probably as dykes. VE. = vertical exaggeration. See
660 location in Fig. 3a.
661
662 Figure 6: Geomorphologic parameters of deep-water volcanoes (gray solid circles; this study),
663 shallow-water volcanoes (pink squares; Magee et al., 2013), subaerial arc volcanoes (green
664 triangles; Grosse et al., 2009), submarine arc volcanoes (grey cross; Wright et al., 2006) and ocean
665 volcanoes (blue rhombus; Smith, 1988). (a) Height vs diameter; (b) Dip vs diameter; (c) Dip vs
666 height; (d) Diameter vs volume; (e) Height vs volume; (f) Dip vs volume; The deep-water
667 volcanoes in this study have different trends (slopes) to other types. The errors of geomorphologic
668 parameters of volcanoes in the study area are from the ranges of volcano velocities.
669
670 Figure 7: (a)-(f): Geomorphologic characteristics of the craters of deep-water volcanoes in this
671 study. (a) Depth vs diameter (crater); (b) Dip vs diameter (crater); (c) Dip (crater) vs depth; (d)
672 Depth vs volume (crater); (e) Diameter (crater) vs volume (crater); (f) Dip (crater) vs volume
673 (crater). (g)-(i): Geomorphologic characteristics between the volcano edifices and craters of deep-
674 water volcanoes. (g) Height vs depth; (h) Diameter (crater) vs diameter (edifice); (i) Volume
675 (crater) vs volume (edifice); (j)-(l): Geomorphologic characteristics of the total volcanoes. (j)
676 (Height + depth) vs average diameter; (k) (Height + depth) vs total volume; (l) Average diameter
677 vs total volume.
678
679 Figure 8: Volcano growth models. (a) Model of deep-water volcano growth (GP1; purple dashed
680 lines) with preferentially vertical aggradation of the edifice flanks; (b) Model of shallow-water
681 volcano growth (red dashed lines) through a proportional increase in summit height and basal
682 diameter (offshore southern Australia; Magee et al., 2013); (c) Model of shallow-water volcano
683 growth (green dashed lines) where summit height increases, whilst basal diameter remains
684 consistent (offshore southern Australia; Magee et al., 2013); (d) Model of shallow-water and
685 subaerial pioneer cones of hyaloclastite mounds (dark blue dashed lines) where the basal diameter
686 increases, whilst the summit height remains consistent (western Indian rifted margin; Calvès et

al., 2011); (e) Model of subaerial shield volcano growth (orange dashed lines) involving a proportional increase in summit height and basal diameter, which is disrupted by a short stage of preferentially lateral progradation of the edifice flanks (Iceland, Rossi, 1996). (f) The expected trends in summit or basal diameter plotted against volcano volume and average flank dip for all models (a-d).

Figure 9: Cartoon showing proposed three-stage evolution of GP1 volcanoes (see text for details). GP2 volcano growth may be akin to Stage 3. SF1 = Seismic facies 1; SF2 = Seismic facies 2; MP = Possible magmatic intrusions.

Table Caption

Table 1: Geometrical parameters of the edifices and craters of volcanoes. (1) = water depth of the seabed where the volcanoes emplace or emplace underneath it (W.D.); (2) = sediment thickness overlying the buried volcanoes (Th.).

Figure 1

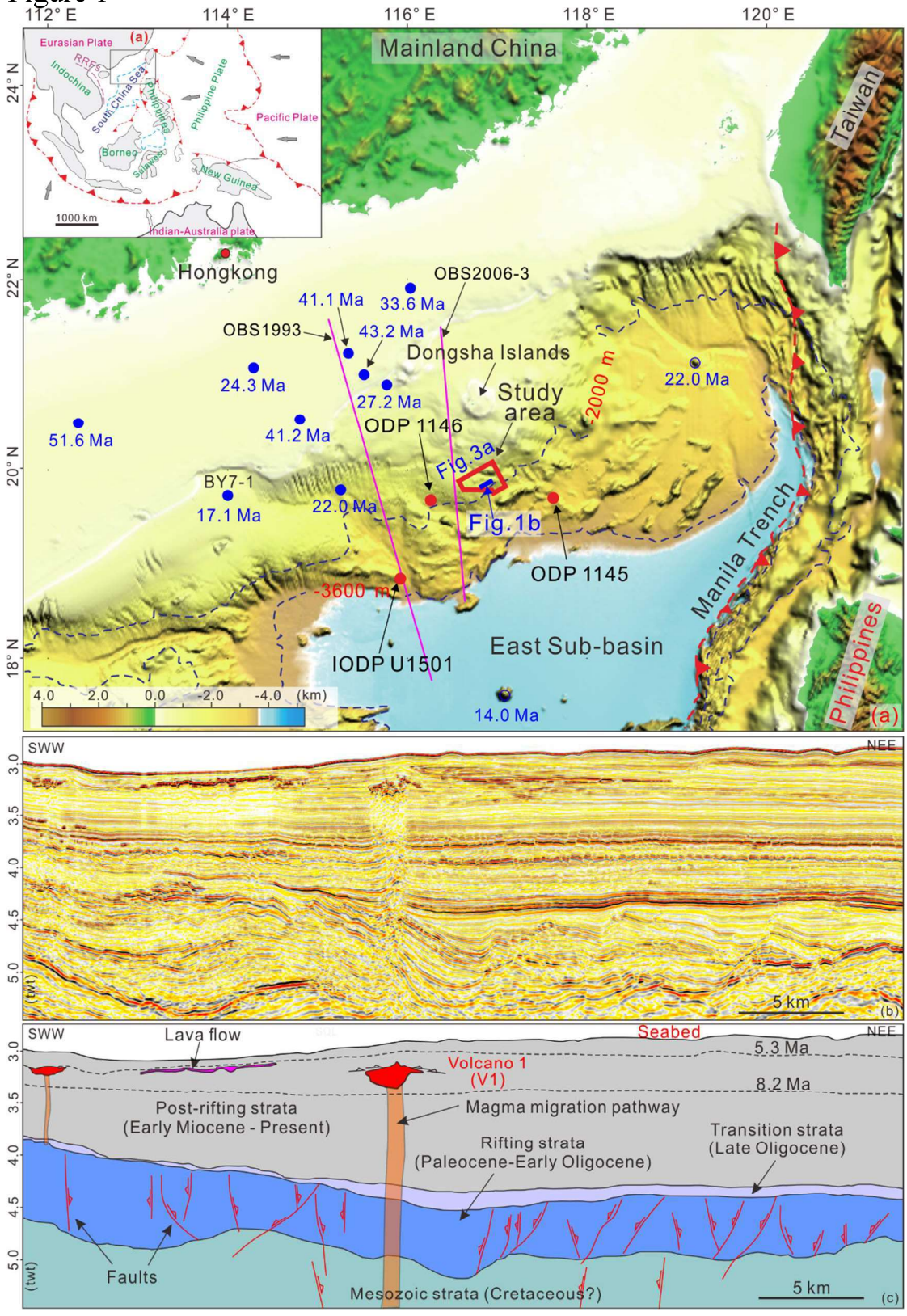
112° E
114° E
116° E
118° E
120° E
24° N
22° N
20° N
18° N
Mainland China
Taiwan
Hongkong
OBS2006-3
41.1 Ma
33.6 Ma
OBS1993
43.2 Ma
Dongsha Islands
24.3 Ma
27.2 Ma
Study area
-2000 m
22.0 Ma
51.6 Ma
41.2 Ma
ODP 1146
Fig.3a
BY7-1
17.1 Ma
22.0 Ma
Fig.1b
ODP 1145
Manila Trench
-3600 m
IODP U1501
East Sub-basin
14.0 Ma
Philippines
(a)
4.0 2.0 0.0 -2.0 -4.0 (km)
Eurasian Plate
Indochina
South China Sea
Philippine Sea
Philippine Plate
Pacific Plate
Borneo
Sulawesi
New Guinea
1000 km
Indian-Australia plate
SWW
NEE
3.0
3.5
4.0
4.5
5.0
(twt)
5 km
(b)
Lava flow
Seabed
5.3 Ma
Volcano 1
(V1)
8.2 Ma
Post-rifting strata
(Early Miocene - Present)
Magma migration pathway
Transition strata
(Late Oligocene)
Rifting strata
(Paleocene-Early Oligocene)
Faults
Mesozoic strata (Cretaceous?)
5 km
(c)

Figure 2

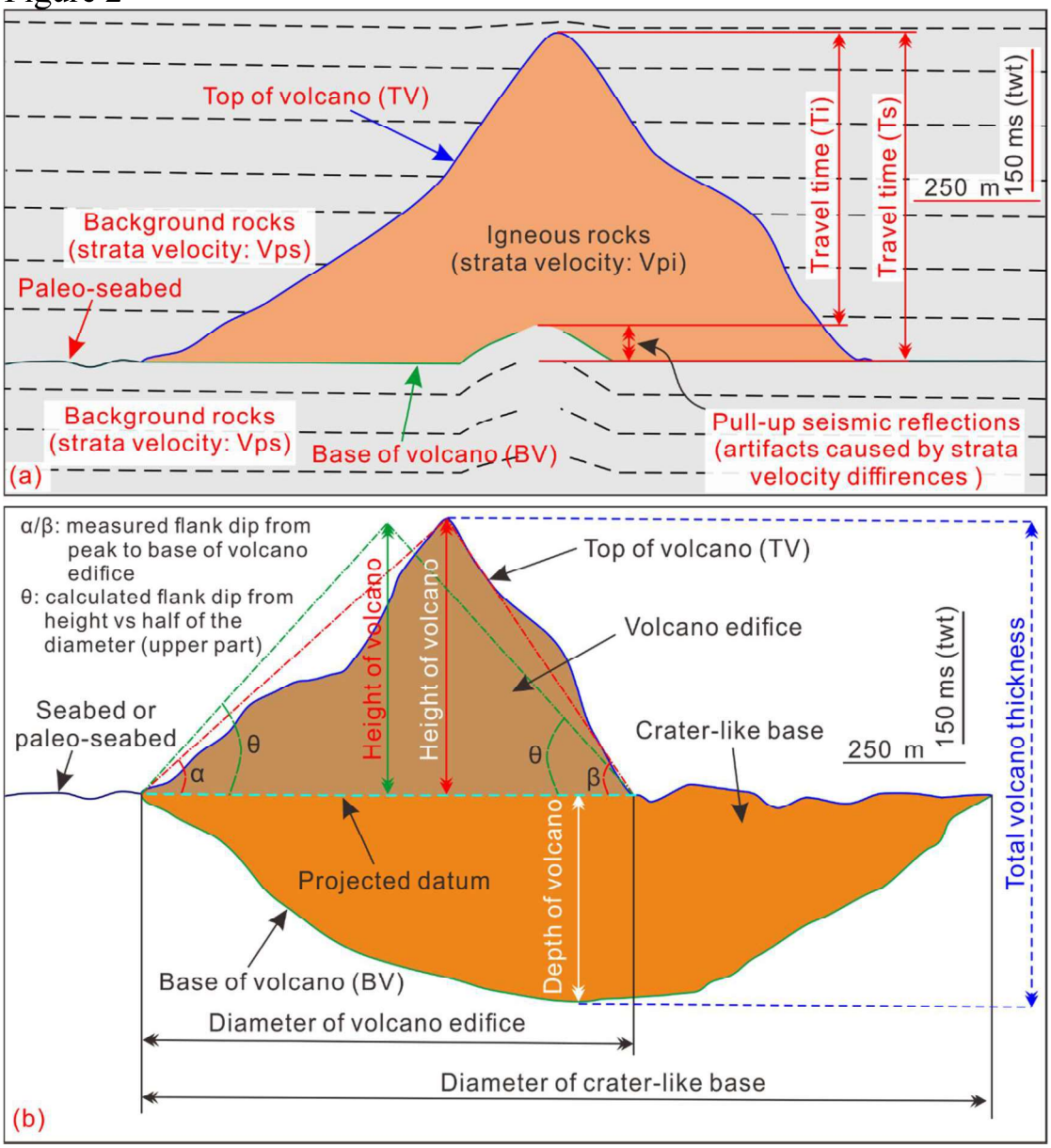
Top of volcano (TV)
Background rocks
(strata velocity: Vps)
Paleo-seabed
Igneous rocks
(strata velocity: Vpi)
Travel time (Ti)
Travel time (Ts)
250 m
150 ms (twt)
Background rocks
(strata velocity: Vps)
Base of volcano (BV)
Pull-up seismic reflections
(artifacts caused by strata
velocity diffirences)
(a)
α/β: measured flank dip from
peak to base of volcano
edifice
θ: calculated flank dip from
height vs half of the
diameter (upper part)
Top of volcano (TV)
Volcano edifice
Height of volcano
Height of volcano
Seabed or
paleo-seabed
θ
α
θ
β
Crater-like base
250 m
150 ms (twt)
Total volcano thickness
Projected datum
Depth of volcano
Base of volcano (BV)
Diameter of volcano edifice
Diameter of crater-like base
(b)

Figure 3

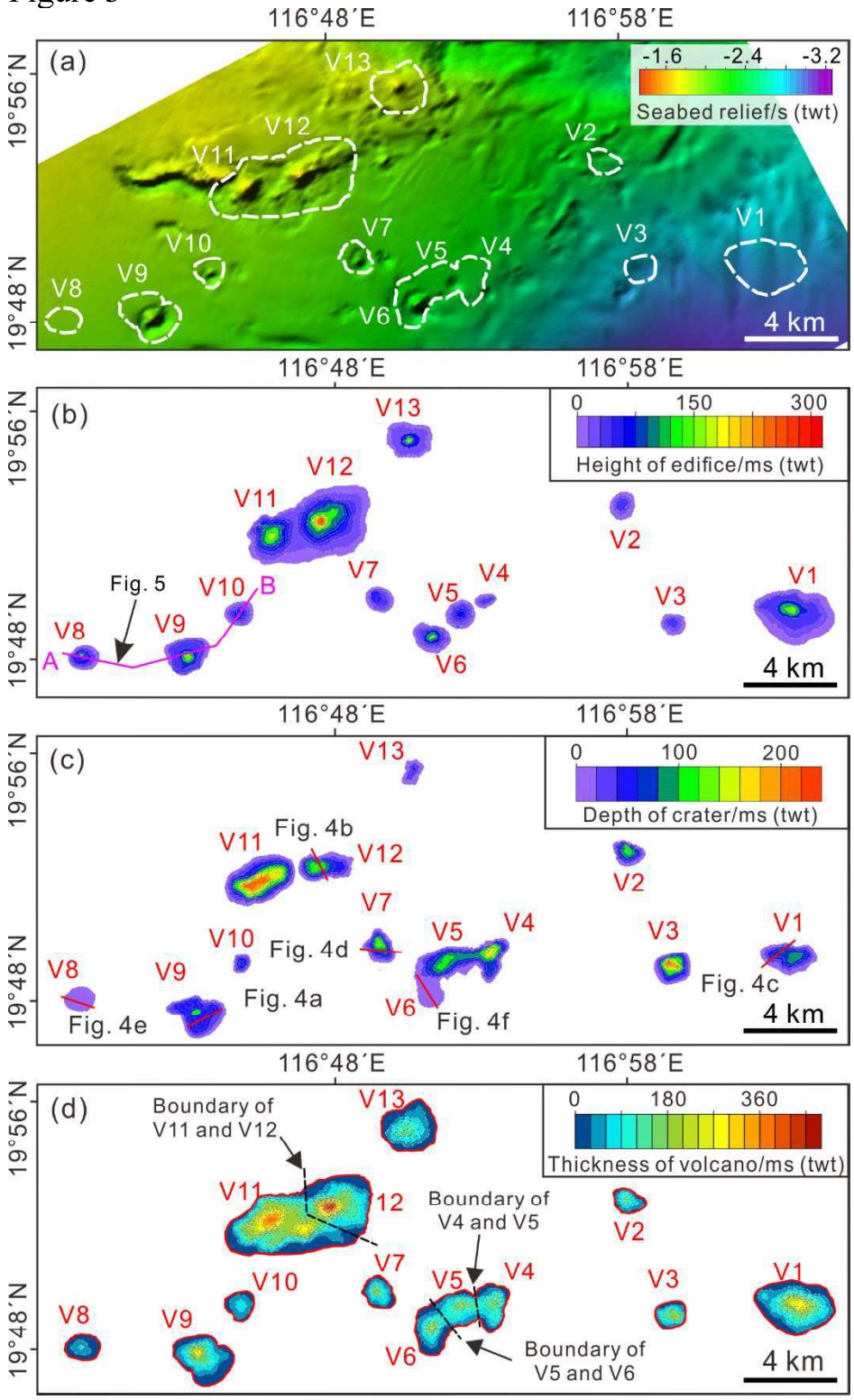
116°48′E
116°58′E
19°56′N
19°48′N
(a)
-1.6
-2.4
-3.2
Seabed relief/s (twt)
V13
V12
V11
V2
V7
V10
V5
V4
V3
V1
V9
V8
V6
4 km
(b)
0
150
300
Height of edifice/ms (twt)
Fig. 5
B
A
(c)
0
100
200
Depth of crater/ms (twt)
Fig. 4b
Fig. 4d
Fig. 4a
Fig. 4e
Fig. 4f
Fig. 4c
(d)
0
180
360
Thickness of volcano/ms (twt)
Boundary of
V11 and V12
Boundary of
V4 and V5
Boundary of
V5 and V6

Figure 4

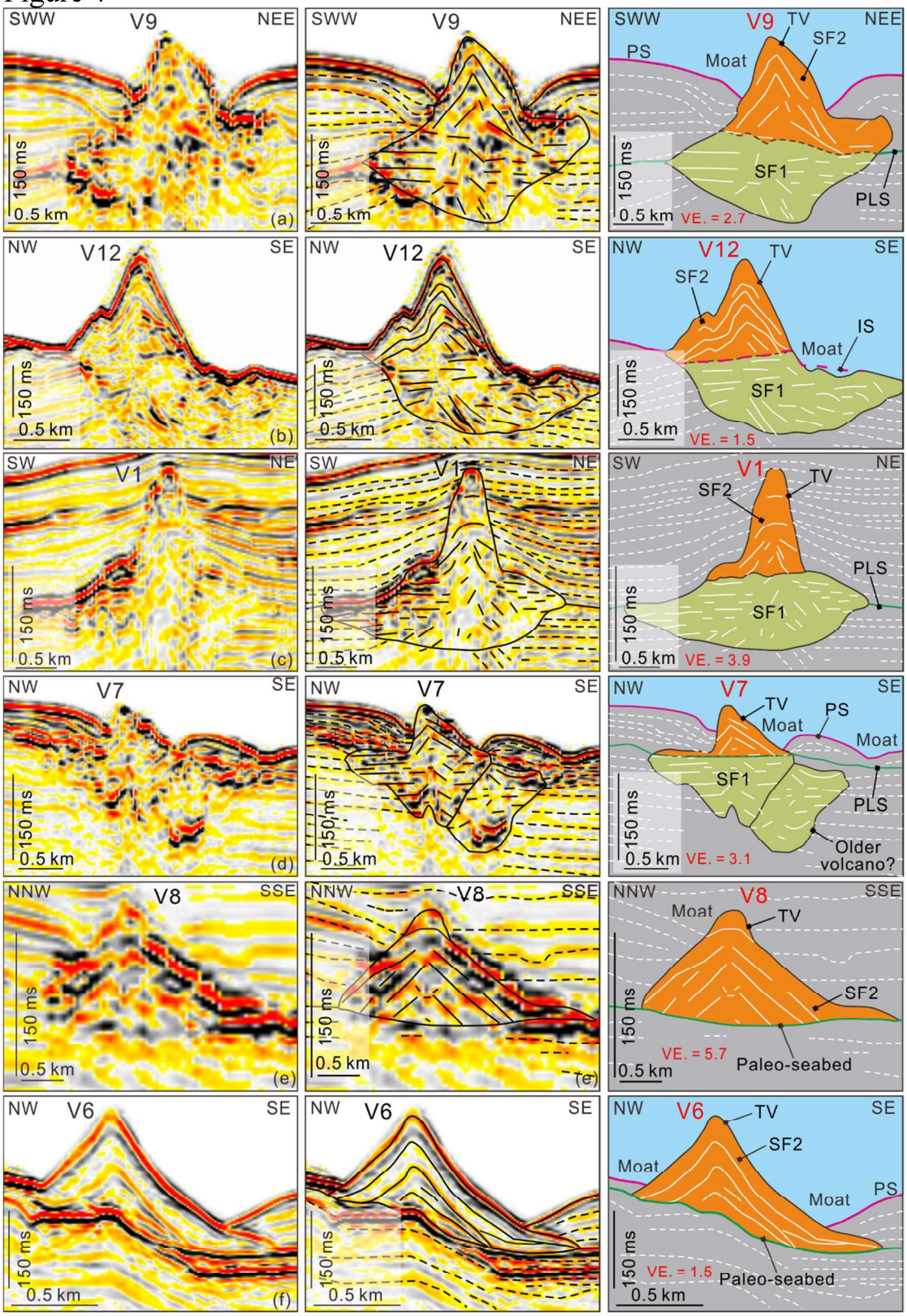
SWW
V9
NEE
150 ms
0.5 km
(a)
PS
Moat
TV
SF2
SF1
PLS
VE. = 2.7
NW
V12
SE
(b)
IS
VE. = 1.5
SW
V1
NE
(c)
VE. = 3.9
NW
V7
SE
(d)
Older volcano?
VE. = 3.1
NNW
V8
SSE
(e)
VE. = 5.7
Paleo-seabed
NW
V6
SE
(f)

714 Figure 5

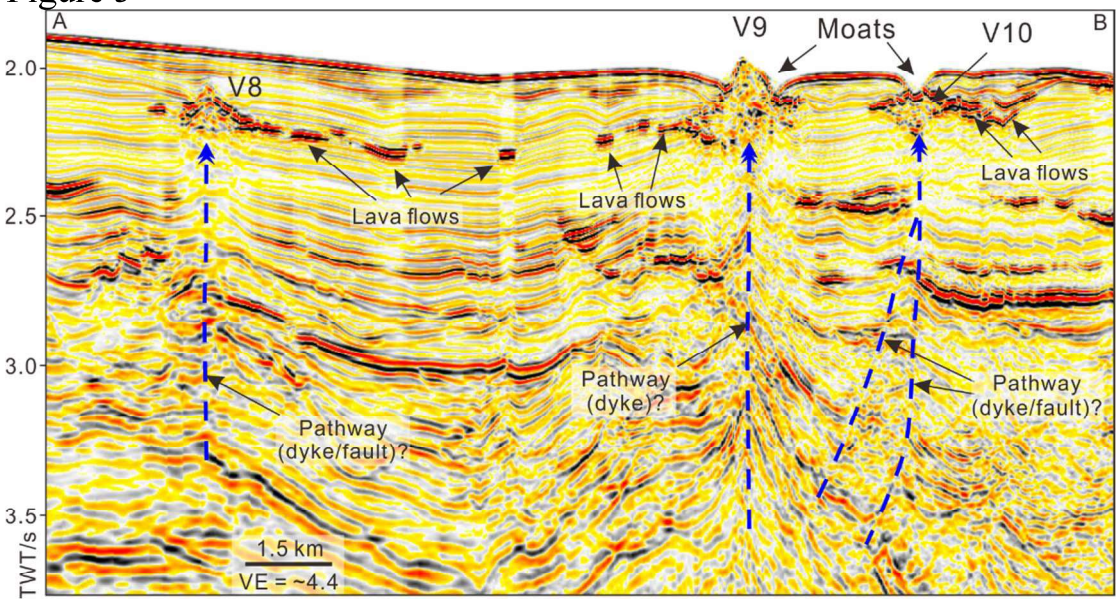

715

716 Figure 6

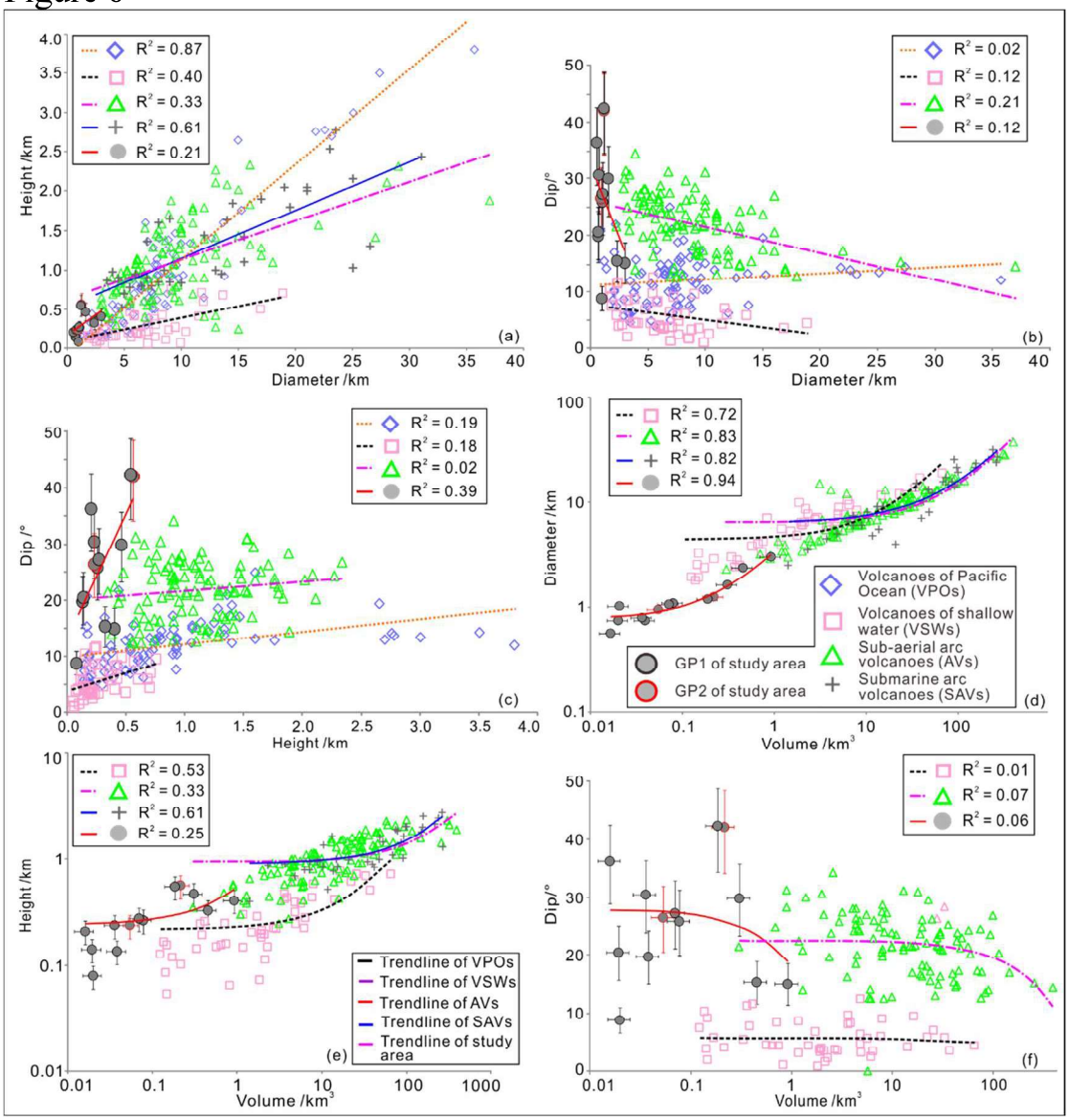

717

718

Figure 7

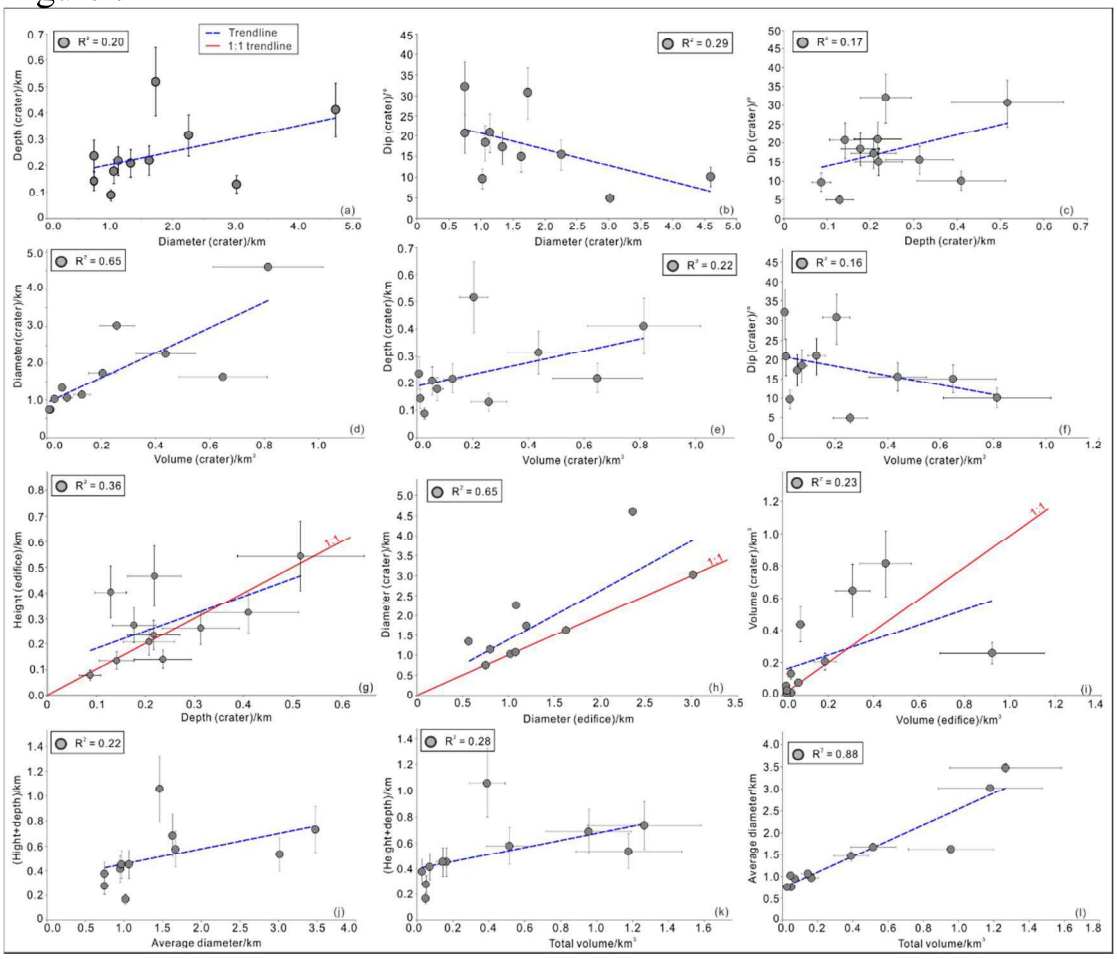
Trendline
1:1 trendline
R² = 0.20
Depth (crater)/km
Diameter (crater)/km
(a)
R² = 0.29
Dip (crater)/°
Diameter (crater)/km
(b)
R² = 0.17
Dip (crater)/°
Depth (crater)/km
(c)
R² = 0.65
Diameter(crater)/km
Volume (crater)/km³
(d)
R² = 0.22
Depth (crater)/km
Volume (crater)/km³
(e)
R² = 0.16
Dip (crater)/°
Volume (crater)/km³
(f)
R² = 0.36
Height (edifice)/km
Depth (crater)/km
1:1
(g)
R² = 0.65
Diameter (crater)/km
Diameter (edifice)/km
1:1
(h)
R² = 0.23
Volume (crater)/km³
Volume (edifice)/km³
1:1
(i)
R² = 0.22
(Hight+depth)/km
Average diameter/km
(j)
R² = 0.28
(Height+depth)/km
Total volume/km³
(k)
R² = 0.88
Average diameter/km
Total volume/km³
(l)

722 Figure 8

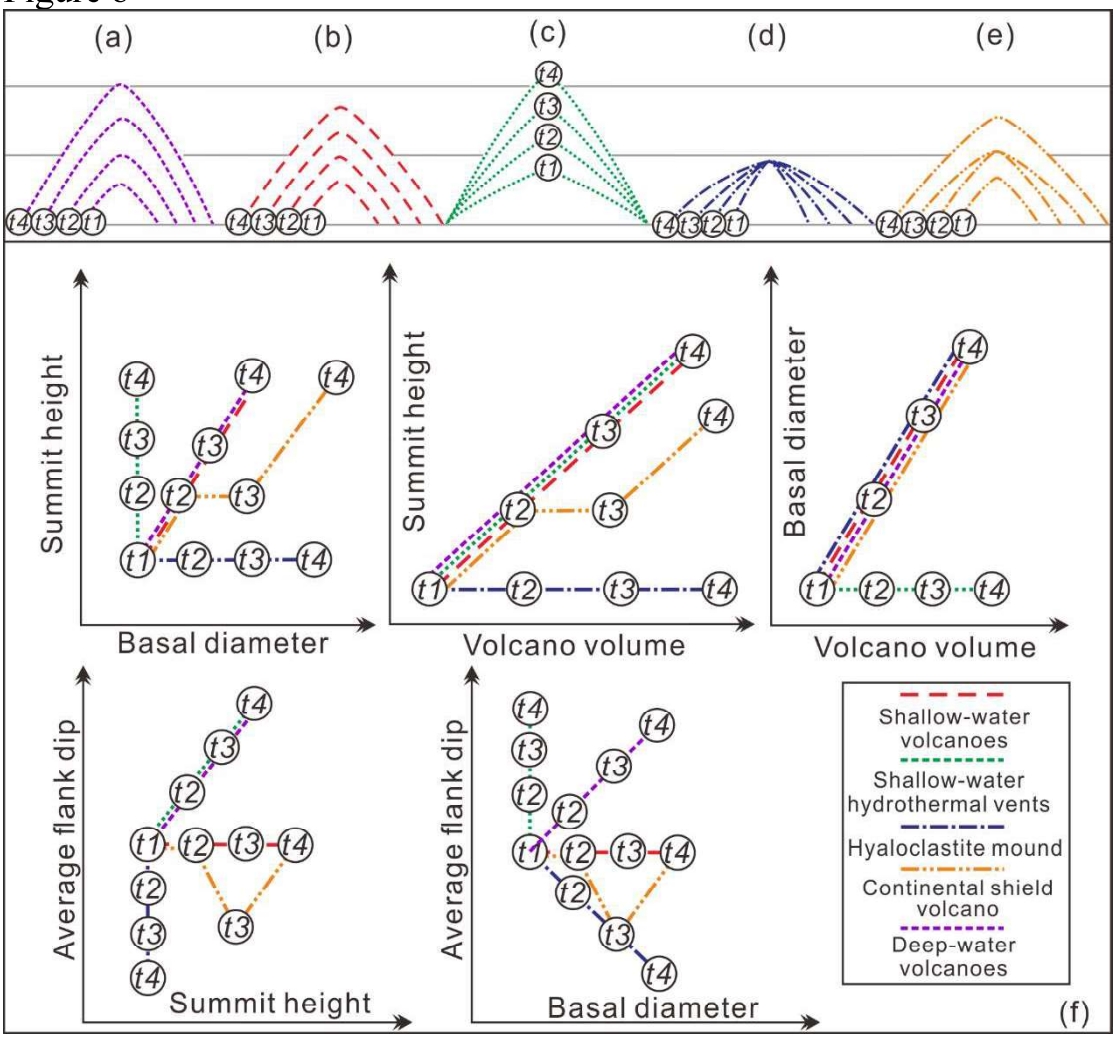

723

724

Figure 9

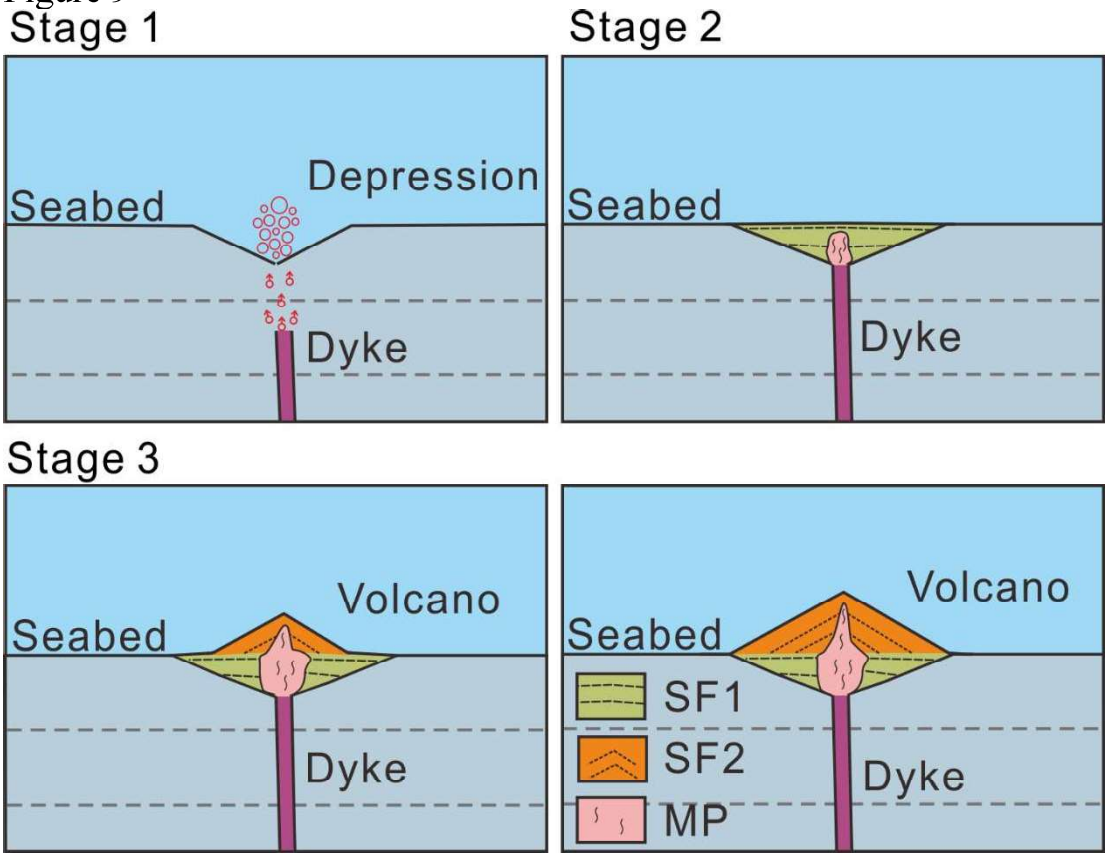
Stage 1
Seabed
Depression
Dyke
Stage 2
Seabed
Dyke
Stage 3
Seabed
Volcano
Dyke
Seabed
Volcano
SF1
SF2
MP
Dyke

Table 1: Geometrical parameters of the edifices and craters of volcanoes. (1) = water depth of the seabed where the volcanoes emplace or emplace underneath it (W.D.); (2) = sediment thickness overlying the buried volcanoes (Th.).

Volcanoes	General parameters		Geometrical parameters of edifices						Geometrical parameters of craters		
No.	W. D./ km(1)	Th./m(2)	Diameter/km	Area/km^2	Height/m	Min. dip/^{o}	Max. dip/^{o}	Volume/km^3	Diameter/km	Depth/m	Volume/km^3
V1	2.25	264.0	3.0	7.15	404±101	11	19	0.92±0.23	3.0	129±32	0.26±0.06
V2	2.14	110.0	0.8	0.44	134±34	15	24	0.04±0.01	0.8	142±35	0.01
V3	2.21	88.0	0.8	0.44	140±35	16	25	0.02	0.8	235±59	0.01
V4	1.83	82.5	0.6	0.25	207±52	29	43	0.02	1.3	208±52	0.06±0.01
V5	1.80	165	1.1	0.92	262±66	20	31	0.08±0.02	2.3	313±78	0.44±0.11
V6	1.65	55.0	1.2	1.21	560±140	34	48	0.22±0.05	--	--	--
V7	1.58	104.5	0.8	0.50	235±59	24	36	0.04±0.01	1.1	217±54	0.13±0.03
V8	1.37	121.0	0.9	0.70	235±59	20	32	0.05±0.01	--	--	--
V9	1.49	247.5	1.6	2.08	467±117	23	36	0.31±0.08	1.6	218±55	0.65±0.16
V10	1.46	115.5	1.0	0.82	79±20	7	11	0.02	1.0	87±22	0.03±0.01
V11	1.37	33.0	2.4	4.37	323±81	12	19	0.45±0.11	4.6	410±103	0.81±0.20
V12	1.35	33.0	1.2	1.12	544±136	34	49	0.19±0.05	1.7	517±129	0.21±0.05
V13	1.36	22.0	1.1	0.89	274±69	21	33	0.07±0.02	1.1	177±44	0.07±0.02